Effect of Surfactant Concentration on the Morphology and Texture of MCM-41 Materials

Gérald Lelong,*,† Sanjib Bhattacharyya,†,|| Steve Kline,‡ Thomas Cacciaguerra,† Miguel A. Gonzalez,§ and Marie-Louise Saboungi*,†

Centre de Recherche sur la Matière Divisée, 1b Rue de la Férollerie 45071 Orléans Cedex 2, France, NIST Center for Neutron Research, National Institute of Standards and Technology, 100 Bureau Drive, Gaithersburg, Maryland 20899-8562, and Instituto de Ciencia de Materiales (CSIC/Universidad de Zaragoza) and Institut Laue-Langevin, 6 rue Jules Horowitz, BP 156 38042 Grenoble Cedex 9, France

Received: January 30, 2008; Revised Manuscript Received: May 27, 2008

Using a simple route for preparing uniform spherical mesoporous MCM-41 materials based on a one-step synthesis in an all-water medium, we have investigated the effects of changes of the surfactant composition. The morphology, texture and structure of five samples with different compositions reveal that both, the external organization and internal pore structure, are governed by the silicate:surfactant ratio. The intake of fluids into the pores—an important issue for the use of this material in biotechnology such as localized drug delivery, vectorization of drugs, biosensing applications, and biochemical separations—was checked and confirmed.

1. Introduction

Following the discovery of mesoporous materials, the synthesis of hierarchically ordered structures has generated a great deal of effort to control simultaneously morphology and texture. Reaction parameters such as solvent, temperature, aging, drying, stirring rates, pH, silica precursor, surfactant type, and the ratio of surfactant to silica play an important role in tailoring the final shape and size of the internal structure for specific applications.[1–13] In the particular case of the MCM-41 type material,[14–17] different chemical mechanisms have been proposed to explain the formation of the various mesostructures: (i) the liquid crystal templating,[18] (ii) the self-assembly,[8,19,20] and (iii) the cooperative self-assembly [8,19–21] mechanisms. Some subtle variations of the reaction parameters and/or the chemical pathways yield different morphologies such as nanospheres, nanorods, tubes, films, fibers, or monoliths.[10,17] The nanospheres are of particular interest due to their potential applications in biochemical separations,[22–24] localized drug delivery,[25–28] and biotechnologies.[17,29,30]

The first spherical mesoporous silica particles were produced via a modification of the Stöber process[31] developed by Grün et al.[32] in which micrometer and submicrometer-size mesoporous spheres were synthesized by adding a freshly distilled silica precursor in an alcoholic solution of diluted surfactant under basic conditions. Since, various chemical synthetical routes have been proposed essentially based on variations of silica sources (e.g., alkoxysilane), of surfactant molecules or templates (e.g., ionic or nonionic molecules, block copolymers,...), of solvents (e.g., alcohol and/or water) and of catalyst (NaOH, NH_4OH,...).[17,33–40]

Marble-like spheres of ~1 nm were produced by Huo et al.[41] using tetrabutyl orthosilicate based on an emulsion biphase route which usually yields hollow mesoporous silica microspheres. Cai et al.[42] synthesized nanoparticles (~100 nm) with an irregular shape in a very dilute solution using NaOH as catalyst, the alkaline solution apparently favoring the formation of shorter micelles compared to an NH_4OH medium. More recently, nanospheres (<200 nm) were obtained by replacing the classical catalysts NaOH and NH_4OH by the polyalcohol triethanolamine.[43] Alcohol was found to have an important influence on both the pore ordering and the spherical morphology of the particles.[44,45] Thus, increasing the ethanol concentration leads to the formation of a succession of mesophases in the order MCM-41, MCM-48, MCM-50 and finally a radial hexagonally ordered phase. The resulting spheres (<1 μm) display a cubic arrangement of the pores in the central region while a hexagonal arrangement is favored in the periphery.[46,47] Another example of the tailoring of morphology and texture by the addition of ethanol has been given by Zhang et al.,[48] who synthesized homogeneous nanospheres (<100 nm) with a radial orientation of the mesopores but without a cubic arrangement in their core. An accurate control of the diameter of the silica spheres can also be achieved by varying the alcohol:water ratio or the type of alkoxysilane.[49] To be complete, mesoporous spheres can also be obtained in an acidic medium by substituting HCl for ammonia,[50–52] with mixtures of surfactant[51,52] or a polymer as template,[53] or by using a spray-drying route.[54–57]

In spite of the large number of studies made on mesoporous materials, complete control of the final spherical morphology and the texture has not yet been fully achieved. It remains crucial to examine in detail the role of the different reaction parameters on the final products. Here we report a detailed study of the effects of the surfactant concentration on the morphology and texture of MCM-41 silica spheres prepared in a water medium without any cosolvent at very low surfactant concentrations.

2. Experimental Details

2.1. Materials. Cetyltrimethylammonium bromide (CTMABr) 99+% as surfactant, tetraethyl orthosilicate (TEOS) 98% as source of silica and aqueous ammonia (reagent grade 30 wt

* Author to whom correspondence should be addressed. E:mail: lelong@cnrs-orleans.fr; mls@cnrs-orleans.fr.

† Centre de Recherche sur la Matière Divisée.

‡ NIST Center for Neutron Research, National Institute of Standards and Technology.

§ Instituto de Ciencia de Materiales (CSIC/Universidad de Zaragoza) & Institut Laue-Langevin.

|| Present address: Center for Bioactive Materials & Tissue Engineering, Bioengineering Department, University of Pennsylvania, Philadelphia, PA 19104.

10.1021/jp800898n CCC: $40.75
Published on Web 06/27/2008

TABLE 1: MCM-41 Samples: Composition of the Starting Materials and Description of the Products

samples	composition				product
MCM-5%	141.2 (H_2O)	2.8 (NH_3)	0.37 (CTMABr)	1 (TEOS)	mesoporous silica with wormlike pores
MCM-2.3%	141.2 (H_2O)	2.8 (NH_3)	0.15 (CTMABr)	1 (TEOS)	μm-scale MCM-41 domains
MCM-1%	141.2 (H_2O)	2.8 (NH_3)	0.07 (CTMABr)	1 (TEOS)	irregular nm-scale MCM-41 particles
MCM-0.5%	141.2 (H_2O)	2.8 (NH_3)	0.035 (CTMABr)	1 (TEOS)	heterogeneous nm-scale MCM-41 spheres
MCM-0.1%	141.2 (H_2O)	2.8 (NH_3)	0.007 (CTMABr)	1 (TEOS)	homogeneous nm-scale MCM-41 spheres

%) purchased from Acros Organics, Merck, and Carlo Erba, respectively, were used as received; the water was purified by distillation and deionization.

2.2. Synthesis. Typical one-step synthesis of ordered MCM-41 silica materials, described by Grün et al.,[58] was used without any alcohol as cosolvent. Five different samples were prepared with the following starting molar compositions: 1TEOS: xCTMABr:2.8NH_3:141.2H_2O, where $x = 0.37, 0.15, 0.07, 0.035$ and 0.007. These molar ratios can also be expressed in weight percentages of surfactant $q_{CTAMBr} = 0.1\%$, 0.5%, 1%, 2.3% and 5% respectively, taking into account only the weights of water and CTMABr. (see Table 1). To produce the 0.1% composition, 0.025 g of CTMABr was dissolved into 25 mL of deionized water and the solution was stirred (~400 rpm) at 60 °C until it became transparent. The pH of the solution was increased to 11.6 by adding 1.56 g of aqueous ammonia. The solution was then heated to 80 °C and 2.08 g of TEOS was added, drop by drop. A white precipitate appeared instantaneously and the solution was then vigorously stirred for 1 h, and placed in an autoclave at 100 °C overnight. The resulting material was recovered by filtration, washed with deionized water, oven-dried at 100 °C for 24 h and finally calcined at 550 °C for 4 h under air flow to remove the template. The same procedure was followed for all compositions.

2.3. Characterization. Transmission electron microscopy (TEM) (Philips-CM20) and powder X-Ray diffraction (XRD) (Philips PW1830) with Cu Kα radiation ($\lambda = 0.154$ nm) were used to determine the texture, morphology and structure. In order to determine the molar ratio Si:CTMABr before calcination, thermo-gravimetric analysis (TG) were performed with a Setaram TG-DTA 92−18 instrument. The samples were heated up to 700 °C at 10 °C/min in an argon atmosphere.

Nitrogen adsorption/desorption isotherms were recorded at liquid nitrogen temperature (77 K) on a Micromeritics ASAP 2010 M gas adsorption system. The samples were outgassed at 473 K for 48 h before measurements. The N_2 isotherms were used to calculate the specific surface area S_{BET}, total pore volume V_T, and pore size distributions.

For the small-angle neutron scattering (SANS) experiments, the 2 mm thick samples were sandwiched between two quartz windows. The measurements were performed at room temperature on the NG-3 and NG-7 30 m SANS instruments[59] at the NIST Center for Neutron Research (Gaithersburg, MD) at an incident wavelength $\lambda = 6$ Å. Detector distances of 1.3, 4, and 13 m were used sequentially to cover a large range of the scattering vector $Q = 0.0035-0.47$ Å^{-1}.

Quasi-elastic neutron scattering (QENS) experiments were performed on the backscattering spectrometer IN16 of the Institute Laue-Langevin (Grenoble, France) at $\lambda = 6.27$ Å with an energy resolution of ≈ 0.9 μeV and covering a Q range of 0.4 to 2 Å^{-1}. The sample contained in a standard flat aluminum holder was impregnated by D_2O, cooled to 10 K for 30 min and heated to 180 K at a rate of 1.4 K.min^{-1}, and to 300 K at a rate of 0.4 K.min^{-1} to ensure full equilibration. While the SANS technique provides a complementary determination of the texture, morphology and organization of the mesoporous samples, the QENS technique enables us to check whether water penetrates into the pores and provides a quantitative information about the confined water dynamics.

3. Experimental Results and Discussion

The evolution of morphology and texture of the final product as a function of the initial concentration in CTMABr is shown in Figure 1. The TEM images show clearly that the non-organized worm-like type porosity observed at 5% concentration is progressively replaced by hexagonal packing of cylindrical pores. This textural modification is also accompanied by significant morphological changes. At a surfactant concentration of 2.3%, corresponding to the procedure described by Grün,[58] large domains of channels organized into honeycomb structure are obtained. The pores slightly curved can reach several hundreds nm in length. By decreasing the surfactant concentration to 1%, the wide domains disappear gradually to form smaller particles with a more rounded shape. Nevertheless, the pores, which still show a slight bending along their length, keep their cylindrical shape and their 2D packing. Near 0.5%, the sample is composed essentially of spheres with irregular diameter in the range 80−200 nm. The particle size dispersion obtained by TEM can be fitted by a Gaussian function characterized by a full width at half-maximum (fwhm) of 35 nm and a mean diameter centered on 139 nm. (Figure 2) The presence of a thin layer of amorphous silica on the surface of the particles is detected by the high-resolution TEM micrographs. For the 0.1% concentration close to the critical micellar concentration (CMC), the spherical particles become more homogeneous in size with a smaller mean diameter (~125 nm) and a narrower Gaussian size dispersion fwhm ~ 20 nm. (Figure 2) The internal structure of the spheres, composed of straight or slightly bent cylindrical pores is arranged in a remarkable honeycomb structure. The length of the pores is now dictated by the diameter of the sphere. Our TEM measurements show also that a decrease in the CTMABr concentration leads to an increase in the sphericity.

At low angles, the XRD patterns exhibit three to five Bragg peaks depending on the surfactant concentrations. These peaks correspond to the (100), (110), (200), (210) and (300) reticular planes of an hexagonal packing of the pores, and are typical of MCM-41 type materials. (Figure 3) Three Bragg peaks are obtained for MCM-0.1% due to the limited long-range order of the pores imposed by the relatively small size of the particles while five peaks are present for the MCM-0.5% and MCM-2.3% samples. Above 2.3%, the MCM-41 structure is gradually lost as shown by the disappearance of the Bragg peaks. To be noted is the general decrease of the inter-reticular distance d with increasing surfactant concentration (See Table 2).

The variations of the inter-reticular distance corresponding to the (100) Bragg peak position d_{100} vs surfactant concentration are rather linear indicating a continuous evolution of the internal structure. (Figure 4) In the particular case of a MCM-41

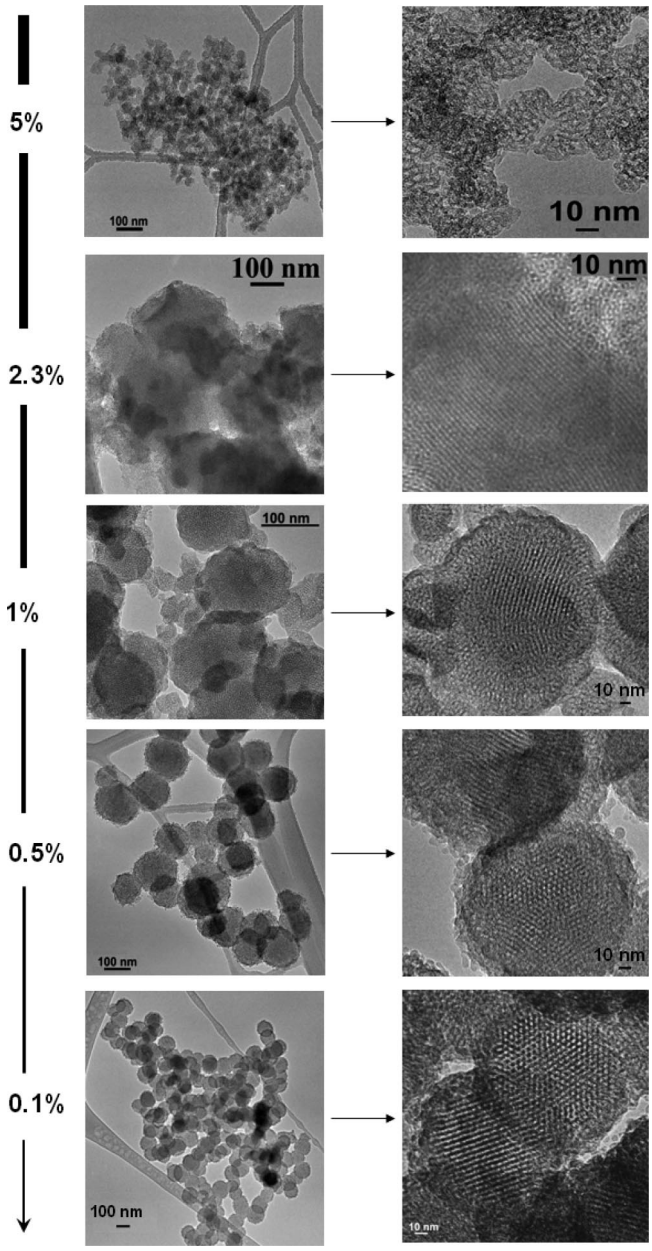

Figure 1. TEM micrographs showing the evolution of the morphology and texture of the mesoporous silica with decreasing CTMABr concentration. The tube like images come from the carbon supporting grids.

structure, the distance between two neighboring pores a_0 can be determined from the relation: $a_0 = (2/\sqrt{3})d_1$. Values of a_0 of 4.21, 4.49, 4.57, and 4.69 nm were obtained for surfactant concentrations of 2.3, 1, 0.5, and 0.1% respectively. Thus, the trend to more perfect spherical shape is accompanied by an increase of the distance between pores possibly due to an increase of the pore wall thickness.

To check the latter possibility, N_2 sorption isotherms of spherical samples of MCM-0.1% and MCM-0.5% were measured. The obtained adsorption/desorption isotherms show a type IV isotherm according to the IUPAC nomenclature (Figure 5).[60] A linear increase of absorbed volume at low pressures is followed by a capillary condensation step in N_2 uptake at a relative pressure of $0.25 < P/P_0 < 0.35$ for MCM-0.1% and $0.22 < P/P_0 < 0.32$ for MCM-0.5%, due to the presence of mesopores. For $0.4 < P/P_0 < 0.9$, the two samples show different behavior:

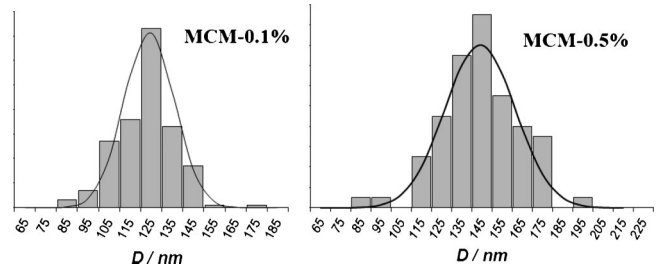

Figure 2. Size dispersion of the MCM-0.1% and MCM-0.5% samples. The lines represent the Gaussian functions centered respectively at 125 and 139 nm.

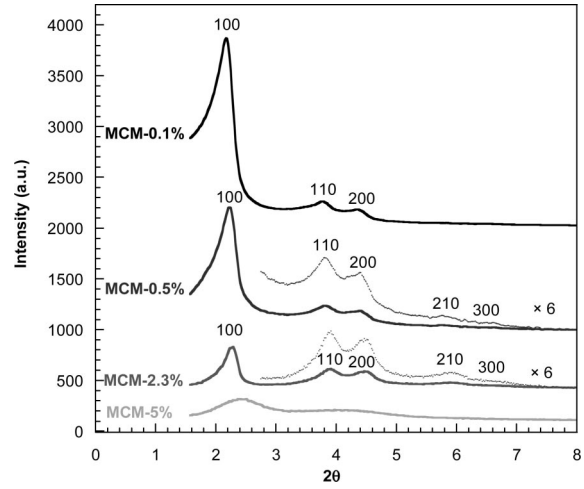

Figure 3. X-ray diffraction patterns of the MCM samples obtained after calcination at 550 °C.

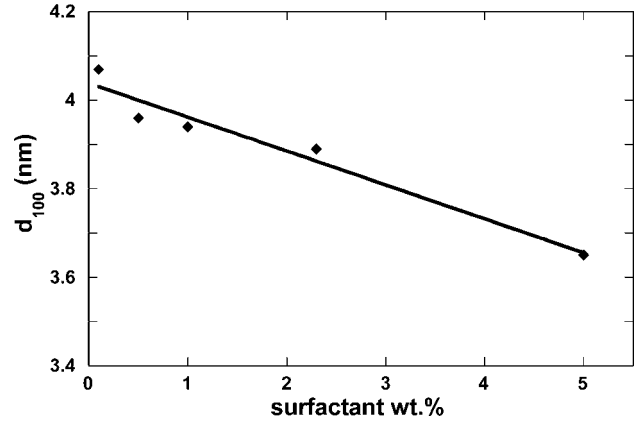

Figure 4. Distance d_{100} calculated from the (100) peak position vs the surfactant concentration. The solid line represents a linear fit.

(i) The isotherm for MCM-0.1% is relatively linear up to $P/P_0 = 0.7$, indicating that the pore size distribution is narrow and unimodal. Above $P/P_0 = 0.9$, a second capillary condensation occurs caused by N_2 adsorption into the empty space formed between the spherical particles.

(ii) In the isotherm for MCM-0.5%, a slight increase of N_2 uptake is visible after the first capillary condensation followed by a small loop for $0.6 < P/P_0 < 0.8$, indicating a bimodal pore distribution.

The parameters obtained listed in Table 3 show that MCM-0.1% presents a mean pore diameter of 3.2 nm with a narrow size dispersion, while MCM-0.5% has two distributions of pores: a narrow one centered on 2.9 nm and a broad one around 7.5 nm.

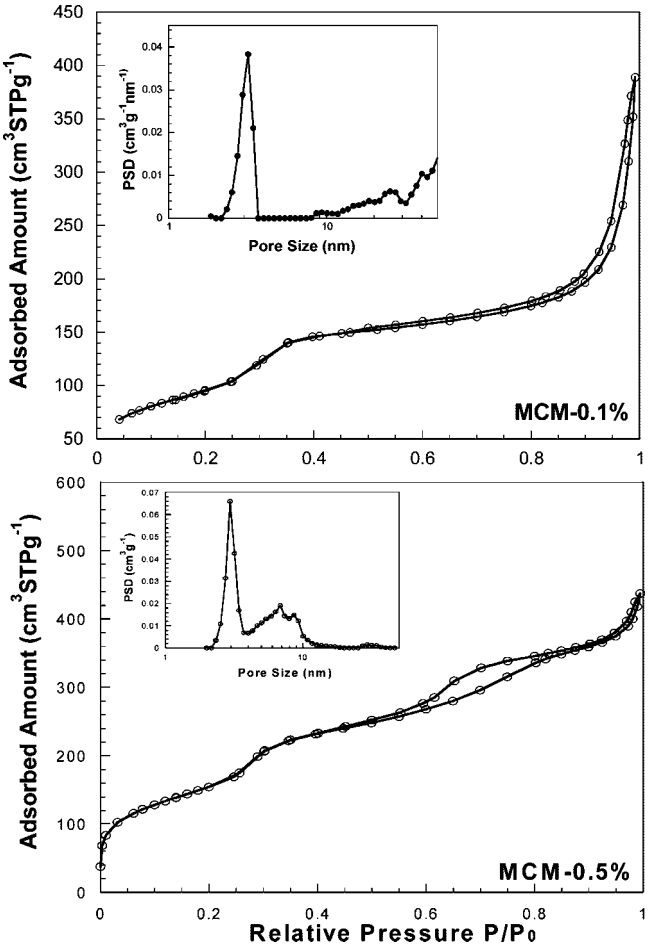

Figure 5. Nitrogen sorption isotherms and the corresponding pore size distributions (insets) measured at 77 K of the MCM-0.1% and MCM-0.5% samples.

TABLE 2: Values of the d_{hkl} Distances Calculated from the XRD Bragg Peaks of the Calcined MCM Samples

	d_{hkl} (nm)			
hkl	0.1%	0.5%	2.3%	5%
100	4.07	3.96	3.89	3.65
110	2.34	2.32	2.26	
200	2.03	2.01	1.97	
210		1.52	1.49	
300		1.34	1.32	

Taking into account the experimental uncertainties, the diameter of the pores appears to be unaffected by the initial amount of surfactant molecules. These results coupled with those from the XRD give an estimation of the pore wall thicknesses around 1.6 nm for MCM-0.1% and MCM-0.5%, which is about 50% higher than those found in the conventional MCM-41 materials (~1 nm),[5] confirming that the pore wall thickness increases with decreasing surfactant concentration. Such behavior can be explained by the change in the Si:CTMABr molar ratio before calcination: at low concentration, rods surrounded by several layers of silica form and aggregate into organic−inorganic cylinders yielding a 2D structure. At higher concentrations, the corresponding amount of silica precursor per surfactant molecule falls down drastically, going from 53 to 10, and condenses around the cylindrical micelles formed by the organic molecules leading to a decrease in the thickness of the silica pore walls. This interpretation is further supported by the observed decrease in the specific surface area from 900−1000 m^2/g for conventional MCM-41[4,58] to 350−570 m^2/g for the spherical nanoparticles.

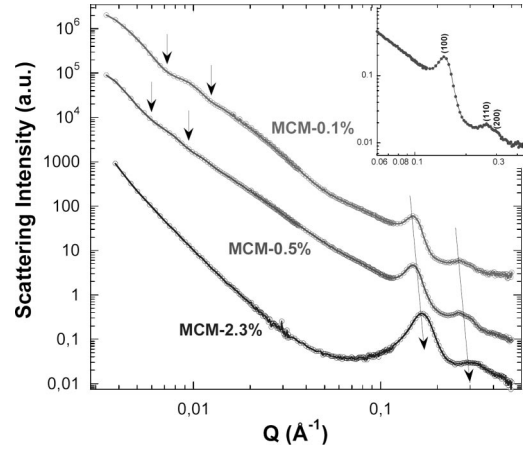

Figure 6. SANS spectra of the MCM-0.1%, MCM-0.5% and MCM-2.3% samples. With increasing surfactant concentration, the oscillations observed in the small-Q region disappear gradually while the Bragg peaks shift to higher Q values. The inset shows an enlargement of the high-Q region for MCM-0.1% showing Bragg peaks corresponding to an hexagonal packing of pores characteristic of the MCM-41 materials.

The morphology and the texture can alternatively be probed by SANS,[61–63] which gives the average structure over a macroscopic region. The scattering intensities for three samples (Figure 6) exhibit features that corroborate the TEM and XRD results. In the low-Q region up to 0.08 $Å^{-1}$, the scattering intensity of the MCM-0.1% sample shows two dips near $Q = 0.0075$ and 0.012 $Å^{-1}$, indicating the presence of spheres with a narrow size dispersion. In the relatively high-Q region, three Bragg peaks are clearly visible at $Q = 0.15$, 0.26 and 0.3 $Å^{-1}$, corresponding to 2θ angles of 2.17°, 3.77° and 4.35° respectively, which are consistent with our XRD results. Also the oscillations observed in MCM-0.1% for $Q < 0.02$ $Å^{-1}$ shift gradually with increasing percentages to smaller Q values indicating an increase of the sphere diameter, before completely disappearing for MCM-2.3%. In the high-Q region, the Bragg peaks shift gradually to larger Q values, indicating a decrease of the distance a_0 and supporting the XRD and BET measurements.

In view of the different particle shapes, length scales and the three-dimensional organization of the pores, a global fit of the scattering function over a large Q range is very difficult to achieve. Nevertheless, morphological and structural information can be deduced from the scattering profile by using appropriate form and structure factors. The form factor of an ideal sphere[64] with a radius r is given by:

$$P_{spheres}(Q) = 9(\Delta\rho)^2 v_{sphere}^2 \left(\frac{\sin(Qr) - Qr\cos(Qr)}{(Qr)^3}\right)^2 \quad (1)$$

and the form factor of a cylinder[64] with a radius r and a length $2H$ is:

$$P_{cylinder}(Q) = \frac{1}{v_{cyl}} \int_0^{\pi/2} \left(2(\Delta\rho) v_{cyl} j_0(QH\cos\alpha) \frac{J_1(Qr\sin\alpha)}{(Qr\sin\alpha)}\right)^2 \sin\alpha \, d\alpha \quad (2)$$

where v_{sphere} and v_{cyl} are the volume of the sphere and cylinder respectively, $v^2(\Delta\rho)^2$ is the contrast, $J_1(x)$ is the first order Bessel function, and α is the angle between the cylinder and the scattering vector Q. The Bragg peaks have been simulated by a Gaussian function $G(Q,\sigma)$. The SANS intensity of the MCM-

TABLE 3: Physico-Chemical Properties of MCM-41 Materials

				N_2 adsorption/desorption			
samples	Si/CTMABr	TEM sphere diameter (nm)	XRD a_0 (nm)	specific surface area (m^2/g)	specific pore volume (cm^3/g)	pore diameter (nm)	wall thickness (nm)
MCM-0.1%	53	125	4.69	350	0.36	3.2	1.5
MCM-0.5%	32	139	4.57	570	0.58	2.9	1.7
MCM-1%	21		4.49			3.2	
MCM-2.3%	10		4.21	1070[a]	0.85[a]	3.2[a]	1.0[a]

[a] Reference 32.

0.1% sample, the form factors of spheres ($r = 60$ nm) and cylinders ($r = 1.7$ nm, length $= 120$ nm) as well as three Gaussian functions centered on 0.15, 0.26 and 0.3 $Å^{-1}$, are shown in Figure 7(a). As expected from our previous observations, the two first minima of $P_{spheres}(Q)$ match the dips of the experimental curve. The oscillations in the low-Q region correspond to spheres with a diameter of 120 nm, which is in perfect agreement with our previous results. $P_{cyl}(Q)$ affects essentially the scattering in the range $0.03\ Å^{-1} < Q < 0.3\ Å^{-1}$. In our simulations, the cylinders have a uniform length of 120 nm, which is not exact but the approximation is reasonable because the cylinder length has a small contribution to the form factor $P_{cyl}(Q)$. Finally, the three Gaussian functions centered at 0.15, 0.26 and 0.3 $Å^{-1}$, coincide well with the XRD data. Since $P_{cyl}(Q)$ plays a role only in the Porod region of $P_{spheres}(Q)$, it is reasonable to approximate the expression of the scattering intensity by the product of a sum of form factors and a sum of structure factors:

$$I(Q) \approx [P_{spheres}(Q) + P_{cylinders}(Q)][1 + G(Q_1, \sigma_1) + G(Q_2, \sigma_2) + G(Q_3, \sigma_3)] \quad (3)$$

Parts b−d of Figure 7 show this function together with the experimental intensities. The agreement is reasonable over the whole Q range, except for $0.1 < Q < 0.3\ Å^{-1}$. To account for the fact that the surface area of the spheres is slightly underestimated, one could introduce a small polydispersity. The low-Q region of the MCM-2.3% sample was fitted by the form factor of polydisperse spheres with a mean diameter of 1 μm, since the ideal case does not apply here. The diameters of the spheres, the size of the cylinders, as well as the position of the Bragg peaks deduced from the simulated $I(Q)$ are presented in Table 4. As expected, we observe a decrease of the sphere diameter, a shift of the Bragg peaks to the higher values of 2θ and a conservation of the pore diameter for decreasing CTMABr concentration. It appears that the diameter of the cylindrical micelles is not affected by changes in the Si:CTMABr ratio corroborating the fact that the dimensions of the micelles are mainly affected by the length of the alkyl chain.

In order to check the intake of aqueous solvent into the pores, QENS measurements were performed on the MCM-0.5% sample filled with D_2O as described in section 2.3. The elastic intensity is proportional to the number of scatterers that are stationary in the time window corresponding to the resolution of the spectrometer, about 2 ns. The temperature scan (Figure 8) shows two well-defined transitions: the first transition around 235 K is due to the confined D_2O [65,66] while the second one around 276 K is due to the melting of bulk deuterated ice. Once we are in the liquid regime, the large mobility of water

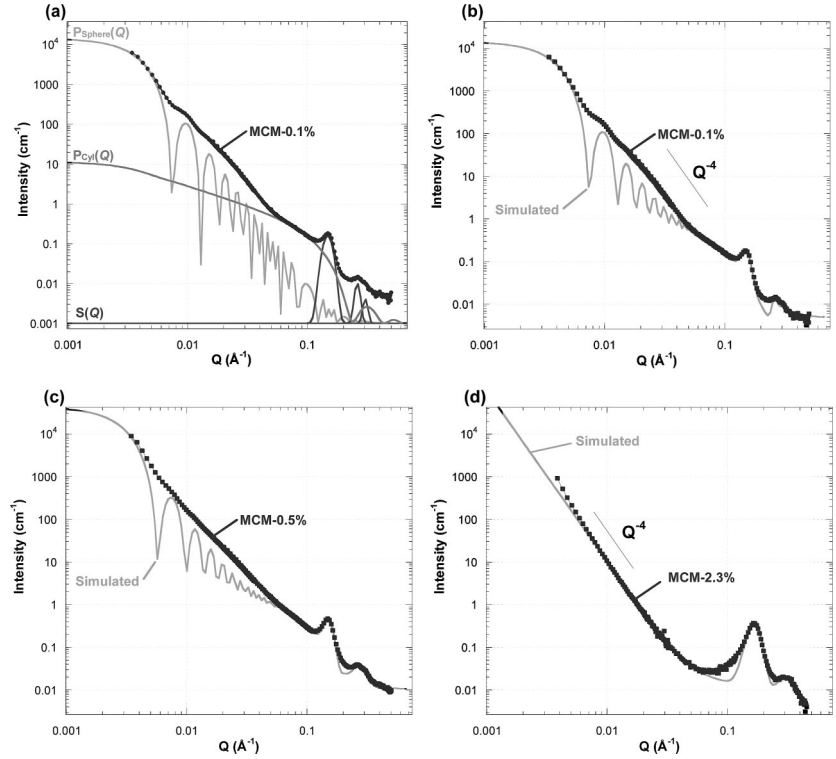

Figure 7. (a) SANS intensity from the MCM-0.1% sample together with the form factors of a cylinder $P_{cyl}(Q)$ and a sphere $P_{sphere}(Q)$. Measured and simulated SANS intensities for the (b) MCM-0.1%, (c) MCM-0.5%, and (d) MCM-2.3% samples.

TABLE 4: Characteristics of the Samples Deduced from the Simulated SANS Spectra

		cylinders		Bragg peaks positions		
sample	spheres diameter (nm)	diameter (nm)	length (nm)	(100) ($Å^{-1}$)	(110) ($Å^{-1}$)	(200) ($Å^{-1}$)
MCM-0.1%	120	3.4	120	0.15	0.26	0.3
MCM-0.5%	160	3.2	160	0.16	0.26	0.3
MCM-2.3%	1000	3.2	300	0.17	0.27	0.32

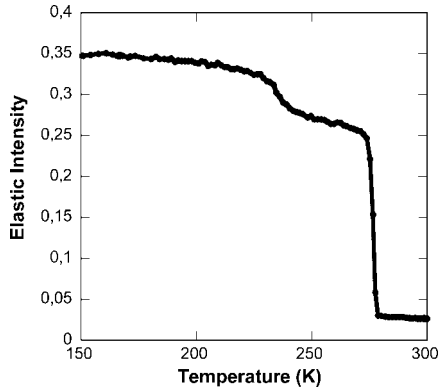

Figure 8. Elastic intensity for MCM-0.5% filled with D_2O. Two transitions are observed: at 276 and 235 K corresponding to the melting of bulk and confined deuterated ice.

molecules causes the elastic signal to disappear almost completely, apart from a small contribution due to the silica matrix. These results confirm that water, and therefore aqueous solutions, can penetrate into the pores of the MCM-41 nanospheres despite the external amorphous silica shell, leading the way to a multitude of applications, especially in catalysis and biotechnology.

Very few papers have reported the formation of nonradial mesoporous nanospheres (~100 nm) in a basic medium in the absence of cosolvents. The most extensive work has been done by Cai et al.[42] who devoted special attention to the role played by the catalyst (NaOH or NH_4OH) role. According to their results, in dilute solution of NaOH, short self-assembled silicate micelles (SSMs) are favored leading to the formation of MCM-41 nanospheres while in the NH_4OH medium, longer SSMs assemble into various nanoforms such as urchin-like agglomerates, submicrometer-sized silica rods, and micrometer-sized oblate silica in terms of the concentration of TEOS or CTMABr. Here, we have formed small spherical mesoporous materials in a NH_4OH medium and confirmed that the concentration of the surfactant molecules and the Si:CTMABr ratio play a major role in controlling the resulting shape and morphology.

4. Concluding Remarks

We propose the following mechanism for the evolution of the nanospheres with the surfactant concentration. For the smallest surfactant concentration (0.1%), the internal hexagonal arrangements of pores are quite pronounced and near to the CMC, the surfactant molecules remain free or poorly organized into dynamic nm-sized spheres or cylinders. In this two-phase system, the positively charged free surfactant molecules present in the water phase become electrostatically adsorbed by the negatively charged silicate oligomers present in the TEOS phase and a water-in-oil type microemulsion occurs.[50] The nucleation and growth of the particles will then fully occur following an order−disorder phase transition as previously reported.[67,68] The small amount of ethyl alcohol generated by the hydrolysis of TEOS acting as a cosurfactant lead to the formation of spherical objects in order to minimize the surface energy. The silicic acid in large excess in the medium will then condense around the mesoporous core leading to the formation of an amorphous silica shell. When the Si:CTMABr ratio is lowered, the mean length of the cylindrical pores and the size of the bundle increase correspondingly. While the amount of TEOS is fixed for all the samples, the ethanol, which is the product of its hydrolysis by water, becomes then less and less efficient as cosurfactant. Consequently, the mesoporous particles will be larger with less rounded shapes, which is consistent with our observations.

In conclusion, we have been able to synthesize mesoporous spherical silica particles with well-defined MCM-41 structures using a very low concentration of surfactant. We also showed the key role that the Si:CTMABr ratio plays on both the texture and the morphology. The resulting size and shape uniformity should prove potentially useful for multiple applications especially in biotechnology and catalysis, or as a template to grow well-aligned nanostructures.[69]

Acknowledgment. This work was supported in part by the Centre National de la Recherche Scientifique, France. G.L. acknowledges the Region Centre for a scholarship SOLEIL. We thank F. Warmont for the BET measurements and Drs. B. Alonso, C.O. Ania, V. Meynen, A. Pineau, and J. Teixeira for helpful discussions. The SANS measurements were carried out at the NIST Center for Cold Neutron Research, which is supported in part by the National Science Foundation under Agreement No. DMR-0086210. Certain trade or names and company products are identified to adequatly specify the experimental procedure. In no case does such identification imply recommendation or endorsement by the National Institute of Standards and Technology, nor does it imply that the products are necessarily best for the purpose.

References and Notes

(1) Shiquan, L.; Cool, P.; Collart, O.; Van Der Voort, P.; Vansant, E. F.; Lebedev, O. I.; Van Tendeloo, G.; Jiang, M. *J. Phys. Chem. B* **2003**, *107*, 10405.

(2) Agren, P.; Linden, M.; Rosenholm, J. B.; Schwarzenbacher, R.; Kriechbaum, M.; Amenitsch, H.; Laggner, P.; Blanchard, J.; Schüth, F. *J. Phys. Chem. B* **1999**, *103*, 5943.

(3) Broyer, M.; Valange, S.; Bellat, J. P.; Bertrand, O.; Weber, G.; Gabelica, Z. *Langmuir* **2002**, *18*, 5083.

(4) Baccile, N.; Grosso, D.; Sanchez, C. *J. Mater. Chem.* **2003**, *13*, 3011.

(5) Cai, Q.; Lin, W.-Y.; Xiao, F.-S.; Pang, W.-Q.; Chen, X.-H.; Zou, B.-S. *Microporous Mesoporous Mat.* **1999**, *32*, 1.

(6) Albuquerque, A.; Vautier-Giongo, C.; Pastore, H. O. *J. Colloid Interface Sci.* **2004**, *284* (2), 687.

(7) Ciesla, U.; Schüth, F. *Microporous Mesoporous Mater.* **1999**, *27*, 131.

(8) Soler-Illia, G. J.; Sanchez, C.; Lebeau, B.; Patarin, J. *Chem. Rev.* **2002**, *102*, 4093.

(9) Moreau, J. J. E.; Vellutini, L.; Wong Chi Man, M.; Bied, C.; Bantignies, J.-L.; Dieudonné, P.; Sauvajol, J.-L. *J. Am. Chem. Soc.* **2001**, *123*, 7957.

(10) Zhao, D.; Yang, P.; Huo, Q.; Chmelka, B. F.; Stucky, G. D. *Curr. Opin. Solid State Mater. Sci.* **1998**, *3*, 111.

(11) Ryoo, R.; Ko, C. H.; Park, I.-S. *Chem. Commun.* **1999**, 1413.

(12) Beck, J. S.; Vartuli, J. C.; Roth, W. J.; Leonowicz, M. E.; Kresge, C. T.; Schmitt, K. D.; Chu, C. T.-W.; Olson, D. H.; Sheppard, E. W.; McCullen, S. B.; Higgins, J. B.; Schlenker, J. L. *J. Am. Chem. Soc.* **1992**, *114*, 10834.

(13) Fontell, K.; Kahn, A.; Lindström, B.; Maciejewska, D.; Puang-Ngern, S. *Colloid Polym. Sci.* **1991**, *269*, 727.

(14) Beck, J. S. US Patent 5,057,296, 1991.

(15) Kresge, C. T.; Leonowicz, M. E.; Roth, W. J.; Vartuli, J. C. US Patent 5,102,643, 1992.

(16) Beck, J. S.; Chu, C. T.; Johnson, I. D.; Kresge, C. T.; Leonowicz, M. E.; Roth, W. J.; Vartuli, J. C. US Patent 5,145,816, 1992.

(17) Bhattacharyya, S.; Lelong, G.; Saboungi, M.-L. *J. Exp. Nanosci.* **2006**, *1* (3), 375.

(18) Kresge, C. T.; Leonowicz, M. E.; Roth, W. J.; Vartuli, J. C.; Beck, J. S. *Nature* **1992**, *359*, 710.

(19) Corma, A. *Chem. Rev.* **1997**, *97*, 2373.

(20) Firouzi, A.; Kumar, D.; Bull, L. M.; Besier, T.; Sieger, P.; Huo, Q.; Walker, S. A.; Zasadzinski, J. A.; Glinka, C.; Nicol, J.; Margolese, D.; Stucky, G. D.; Chmelka, B. F. *Science* **1995**, *267*, 1138.

(21) Patarin, J.; Lebeau, B.; Zana, R. *Curr. Opin. Colloid Interface Sci.* **2002**, *7*, 107.

(22) Zhao, X. S.; Lu, G. Q.; Millar, G. J. *Ind. Eng. Chem. Res.* **1996**, *35*, 2075.

(23) Kisler, J. M.; Dähler, A.; Stevens, G. W.; O'Connor, A. J. *Microporous Mesoporous Mater.* **2001**, *44*−*45*, 769.

(24) Galarneau, A.; Lapichella, J.; Brunel, D.; Fajula, F.; Bayram-Hahn, Z.; Unger, K.; Puy, G.; Demesmay, C.; Rocca, J.-L. *J. Sep. Sci.* **2006**, *29*, 844.

(25) Vallet-Regi, M.; Ramila, A.; Del Real, R. P.; Perez-Periente, J. *Chem. Mater.* **2001**, *13*, 308.

(26) Lai, C.-Y.; Trewyn, B. G.; Jeftinija, D. M.; Jeftinija, K.; Xu, S.; Jeftinija, S.; Lin, V. S.-Y. *J. Am. Chem. Soc.* **2003**, *125*, 4451.

(27) Munõz, B.; Rámila, A.; Pérez-Pariente, J.; Dýaz, I.; Vallet-Regý, M. *Chem. Mater.* **2003**, *15*, 500.

(28) Slowing, I.; Trewyn, B. G.; Lin, V. S.-Y. *J. Am. Chem. Soc.* **2006**, *128*, 14792.

(29) Buranda, T.; Huang, J.; Ramarao, G. V.; Ista, L. K.; Larson, R. S.; Ward, T. L.; Sklar, L. A.; Lopez, G. P. *Langmuir* **2003**, *19*, 1654.

(30) Lin, Y. S.; Tsai, C.-P.; Huang, H. Y.; Kuo, C. T.; Hung, Y.; Huang, D.-M.; Chen, Y.-C.; Mou, C.-Y. *Chem. Mater.* **2005**, *17*, 4570.

(31) Stöber, W.; Fink, A.; Bohn, E. J. *Colloid Interface Sci.* **1968**, *26*, 62.

(32) Grün, M.; Later, I.; Unger, K. K. *Adv. Mater.* **1997**, *9*, 254.

(33) Mou, C. Y.; Lin, H.-P. *Pure Appl. Chem.* **2000**, *72*, 137.

(34) Yang, H.; Vovk, G.; Coombs, N.; Sokolov, I.; Ozin, G. A. *J. Mater. Chem.* **1998**, *8* (3), 743.

(35) Gallis, W.; Araujo, J. T.; Duff, K. J.; Moore, J. G.; Landry, C. C. *Adv. Mater.* **1999**, *11* (17), 1452.

(36) Unger, K. K.; Kumar, D.; Grün, M.; Bückel, G.; Lüdtke, S.; Adam, T.; Schumacher, K.; Renker, S. J. *J. Chromatogr. A* **2000**, *892* (1−2), 47.

(37) Nooney, R. I.; Thirunavukkarasu, D.; Chen, Y.; Josephs, R.; Ostafin, A. E. *Chem. Mater.* **2002**, *14*, 4721.

(38) Ma, Y.; Qi, L.; Ma, J.; Wu, Y.; Liu, O.; Cheng, H. *Colloids Surf. A* **2003**, *229* (1−3), 1.

(39) Yano, K.; Fukushima, Y. J. *J. Mater. Chem.* **2003**, *13*, 2577.

(40) Kumar, D.; Schumacher, K.; du Fresne von Hohenesche, C.; Grün, M.; Unger, K. K. *Colloids Surf. A: Physicochem. Eng. Aspects* **2001**, *187*−*188*, 109.

(41) Huo, Q.; Feng, J.; Schüth, F.; Stucky, G. D. *Chem. Mater.* **1997**, *9*, 14.

(42) Cai, Q.; Luo, Z.-S.; Pang, W.-Q.; Fan, Y.-W.; Chen, X. H.; Cui, F.-Z. *Chem. Mater.* **2001**, *13*, 258.

(43) Möller, K.; Kobler, J.; Bein, T. *Adv. Funct. Mater.* **2007**, *17*, 605.

(44) Liu, S.; Collart, O.; Cool, P.; Van Der Voort, P.; Vansant, E. F.; Minhua, J.; Lebedev, O. I.; Tendeloo, G. V. *J. Phys. Chem. B* **2003**, *107*, 10405.

(45) Shiquan, L.; Lingshao, L.; Zhongxi, Y.; Cool, P.; Vansant, E. F. *Mater. Chem. Phys.* **2006**, *97*, 203.

(46) Van Tendeloo, G.; Lebedev, O. I.; Collart, O.; Cool, P.; Vansant, E. F. *J. Phys. Cond. Matter* **2003**, *15*, S3037.

(47) Lebedev, O. I.; Tendeloo, G. V.; Collart, O.; Cool, P.; Vansant, E. F. *Solid State Sci.* **2004**, *6*, 489.

(48) Zhang, Y.-B.; Qian, X.-F.; Li, Z.-K.; Yin, J.; Zhu, Z.-K. *J. Solid State Chem.* **2004**, *177*, 844.

(49) Yano, K.; Fukushima, Y. J. *Mater. Chem.* **2003**, *13*, 2577.

(50) Schacht, S.; Huo, Q.; Voigt-Martin, I. G.; Stucky, G. D.; Schuth, F. *Science* **1996**, *273*, 768.

(51) Pang, X.; Tang, F. *Microporous Mesoporous Mat.* **2005**, *85*, 1.

(52) Qi, L.; Ma, J.; Cheng, H.; Zhao, Z. *Chem. Mater.* **1998**, *10*, 1623.

(53) Boissière, C.; van der Lee, A.; El Mansouri, A.; Larbot, A.; Prouzet, E. *Chem. Commun.* **1999**, 2047.

(54) Lu, Y.; Fan, H.; Stump, A.; Ward, T. L.; Rieker, T.; Brinker, C. J. *Nature* **1999**, *398*, 223.

(55) Brinker, C. J.; Lu, Y.; Sellinger, A.; Fan, H. *Adv. Mater.* **1999**, *11*, 579.

(56) Bore, M. T.; Rathod, S. B.; Ward, T. L.; Datye, A. K. *Langmuir* **2003**, *19*, 256.

(57) Alonso, B.; Douy, A.; Véron, E.; Perez, J.; Rager, M.-N.; Massiot, D. J. *Mater. Chem.* **2004**, *14*, 1.

(58) Grün, M.; Unger, K. K.; Matsumoto, A.; Tsutsumi, K. *Microporous Mesoporous Mat.* **1999**, *27*, 207.

(59) Glinka, C. J.; Barker, J.; Hammouda, B.; Krueger, S.; Moyer, J.; Orts, W. *J. Appl. Crystallogr.* **1998**, *31*, 430.

(60) IUPAC. Reporting Physisorption Data for Gas/Solid Systems *Pure Appl. Chem.* **1957**, *87*, 603

(61) Edler, K. J.; Reynolds, P. A.; White, J. W. *J. Phys. Chem. B* **1998**, *102*, 3676.

(62) Connolly, J.; Singh, M.; Buckley, C. E. *Physica B* **2004**, *350*, 224.

(63) Dore, J. C.; Webber, J. B. W.; Strange, J. H. *Colloids Surf. A* **2004**, *241*, 191.

(64) Kline, S. R. *J. Appl. Crystallogr.* **2006**, *39*, 895.

(65) Floquet, N.; Coulomb, J.-P.; Dufau, N.; Andre, G.; Kahn, R. *Adsorption* **2005**, *11*, 139.

(66) Schreiber, A.; Ketelsen, I.; Findenegg, G. H. *Phys. Chem. Chem. Phys.* **2001**, *3*, 1185.

(67) Sadasivan, S.; Fowler, C. E.; Khushalani, D.; Mann, S. *Angew. Chem., Int. Ed.* **2002**, *41*, 2151.

(68) Chan, H. B. S.; Budd, P. M.; de, V.; Naylor, T. *J. Mater. Chem.* **2001**, *11*, 951.

(69) Slowing, I. I.; Trewyn, B. G.; Giri, S.; Lin, V. S.-Y. *Adv. Funct. Mater.* **2007**, *17*, 1225–1236.

JP800898N